Interaction of advancing contact lines with defects on heated substrates

Vladimir S. Ajaev,[1,*] Elizaveta Ya. Gatapova,[2,3] and Oleg A. Kabov[2,3]
[1]*Department of Mathematics, Southern Methodist University, Dallas, Texas 75275, USA*
[2]*Kutateladze Institute of Thermophysics SB RAS, Lavrentyev Ave., 1, Novosibirsk, 630090, Russia*
[3]*Novosibirsk State University, Novosibirsk, 630090, Russia*

(Received 31 October 2019; accepted 23 January 2020; published 18 February 2020)

We consider an advancing contact line traveling over a region of locally modified wetting or thermal substrate properties. A lubrication-type model is developed to account for coupling of viscous flow, evaporation, surface tension, and disjoining pressure. Stick-slip-type behavior is found for a range of conditions as the contact line passes over the defect and explained by a temporary increase in the local stresses disrupting the liquid supply into the contact line region. A simple estimate of the degree of contact line slowdown is obtained and compared with the numerical simulation results. Tangential stresses arising from the action of the electric field on the interfacial changes are accounted for in our model; neglecting them would lead to an overprediction of the time of interaction between the contact line and the defect. Increasing the substrate temperature uniformly has little effect on contact line motion, but local increase of the temperature enhances the tendency of the contact line to be pulled back by the defect, an effect explained by the Marangoni stresses.

DOI: 10.1103/PhysRevE.101.022801

I. INTRODUCTION

Moving contact lines on heated surfaces appear in many applications such as spray cooling [1,2], boiling [3–5], heat pipes [6,7], and fuel cells [8]. In the context of the present work, we define a contact line as a line along which a liquid-gas interface comes into contact with a flat solid substrate based on macroscale observations. This definition includes the case of the so-called apparent contact line, corresponding to a situation when the solid is covered with an ultrathin wetting film but still appears dry on macroscale. The existence of adsorbed films in confined liquid-vapor systems was verified in several careful experimental studies [9,10]. The experimental results are consistent with the predictions of theoretical models originated in the classical works of Potash and Wayner [11] and Moosman and Homsy [12].

The challenges in mathematical modeling of moving contact lines stem from coupling of the effects of phase change, surface tension, viscous flow, and substrate wetting properties. Numerous studies of moving contact lines on heated substrates are a subject of recent comprehensive review articles [13,14]. Here we focus on a special case of when the solid substrate is spatially heterogeneous due to nonuniformity of either the local wetting properties or local temperature. Our interest stems from both the fundamental issue of how substrate imperfections affect contact line motion and heat transfer applications in which patterned and structured surfaces have been increasingly used for heat transfer enhancement for a variety of configurations [15].

Experimental studies of dynamic contact lines on heterogeneous surfaces reported a phenomenon of the so-called stick-slip motion in which a contact line remains stationary for a period of time and then rapidly advances until suddenly coming to a halt again [16]; the process is then repeated periodically. Quantitative modeling of this phenomena is a difficult problem, since an attempt to impose a contact angle, i.e., specify the angle between the local tangent to the fluid interface and the substrate, leads to a nonintegrable shear-stress singularity [17,18]. The presence of ultrathin precursor films ahead of advancing contact lines on spatially homogeneous nonheated substrates, detected in a number of experimental studies [19,20], has been suggested as a possible physical mechanism for removing the singularity [17]. However, alternative mechanisms for removing the singularity have been proposed in the literature, e.g., hydrodynamic slip at the liquid-solid interface [21,22]. The slip models have been implemented in several elaborate numerical studies [23,24].

A novel approach to overcoming the challenge of describing contact line motion over *heterogeneous* substrates was introduced in the works of Schwartz [25] and Thiele *et al.* [26,27]. Instead of imposing a contact angle condition, these authors describe substrate heterogeneity using spatially varying disjoining pressure. The concept of disjoining pressure, introduced in the pioneering works of Derjaguin *et al.*, is used to account for unbalanced intermolecular interactions and a number of other physical effects which become important when liquids are confined between two interfaces which are very close to each other, typically at a distance of about 100 nm or less [28,29]. While initially developed for perfectly wetting liquids, the disjoining pressure approach was later successfully applied to situations when the macroscopic contact angle is not zero but the solid substrate is still covered by an ultrathin film, a configuration often referred to as pseudopartial wetting [30,31]. For water and aqueous solutions, the disjoining pressure is usually approximated by a two-component expression [28,32], where the first component accounts for London–van der Waals dispersion forces,

*ajaev@smu.edu

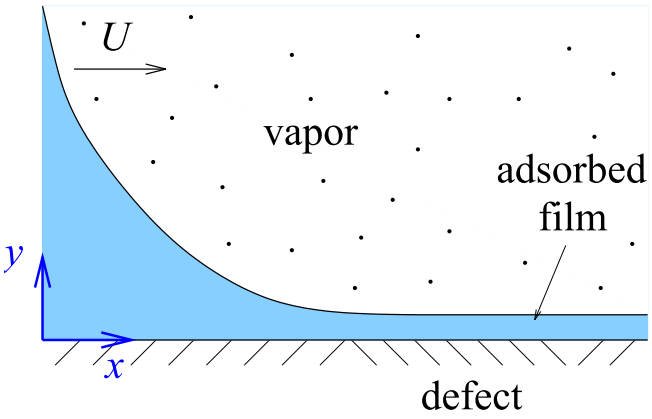

FIG. 1. Sketch of an apparent contact line advancing towards a substrate defect.

while the second one has to do with electrostatic interactions due to electrical charges at the solid-liquid and liquid-gas interfaces and the rearrangement of ions in the liquid. The two-component disjoining pressure approach allowed Thiele and Knobloch [26] to uncover rich bifurcation dynamics associated with pinning and depinning of droplets moving under external forcing, such as gravity. However, no phase change at the interface was considered by these authors.

The approach of Thiele *et al.* [26,27] was first applied to situations with evaporation in our recent study [33]. However, that work was mostly focused on the heat transfer aspects of the problem and only dealt with receding contact lines. Furthermore, it had two important limitations: the assumption of uniformity of the substrate temperature and neglect of the component of the shear stress at the interface due to action of the electric field on the interfacial charges [34]. In the present study we overcome both of these limitations.

II. FORMULATION

We consider a configuration of a liquid meniscus advancing in a capillary at a controlled speed, see Fig. 1. The liquid phase has density ρ and viscosity μ, the gas phase is assumed to be pure vapor of the same liquid, and the surface tension at the interface is σ. This configuration is directly relevant to the situation when a liquid plug is moving in pulsating heat pipes [6] and some flow boiling configurations [35], but can also be thought of as a simple model system for fundamental studies of interaction of advancing contact lines with substrate heterogeneities.

The starting point for our analysis is the general system of Navier-Stokes, continuity, and energy equations coupled to the equation describing the electrostatic effects. A number of simplifications are made to these equations using the ideas from the standard lubrication-type analysis [36–40]. It is convenient to outline these simplifications using nondimensional variables.

Let us discuss the choice for nondimensional velocities and coordinates. There are clearly two characteristic velocities in the problem. The first one is the dimensional velocity of forced motion of the meniscus U^*, controlled experimentally by, e.g., changing the pressure gradient in the capillary tube. The second one, denoted by U_e, is related to the flow which supports the evaporation process at the interface. If the limiting factor for the rate of phase change is the supply of heat to the interface and the superheat is given by ΔT, this velocity can be estimated as $U_e = k\Delta T/\rho\mathcal{L}R_0$, where k is the thermal conductivity of the liquid, $\mathcal{L}$ is the latent heat, and R_0 is the length scale set by the macroscopic geometry away from the contact line, e.g., the radius of curvature of a meniscus moving in a channel. Either U^* or U_e could be used as the velocity scale; we use the latter to facilitate easier comparisons with several recent studies [33,40]. The capillary number based on this velocity, $\mathrm{Ca} = \mu U_e/\sigma$, is typically very small, allowing one to use asymptotic methods to describe the apparent contact line region. Specifically, the lubrication-type model we are using is applicable when $\mathrm{Ca} \ll 1$ and the vertical length scale is much smaller than the horizontal one. Under these conditions, the local balance of viscous and capillary forces leads to the well-known Landau-Levich-Bretherton scaling [38,41]. In the present framework, this implies using $\mathrm{Ca}^{1/6}R_0$ and $\mathrm{Ca}^{1/3}R_0$ as the scales for the Cartesian coordinates x and y, respectively. We note that there is also another length scale in the problem, the Debye length defined by

$$\lambda_D = \sqrt{\frac{\epsilon k_B T^*}{e^2 \sum_{k=1}^{N} n_k^{(0)} z_k^2}}, \tag{1}$$

where ϵ is the electric permittivity of the liquid, k_B is the Boltzmann constant, and T^* is the dimensional temperature; we assume that the liquid contains N different types of ions of valencies z_k and bulk concentrations $n_k^{(0)}$ $(k = 1, 2, \ldots, N)$. Since the electrostatic effects make a substantial contribution to the disjoining pressure only when the electrical double layers formed near the interfaces overlap, we assume the Debye length to be of the same order of magnitude as the film thickness. In our formulation this corresponds to the assumption of the ratio $\kappa = \mathrm{Ca}^{1/3}R_0/\lambda_D$ being an order one quantity in the asymptotic limit of $\mathrm{Ca} \to 0$. This is a reasonable assumption due to small values of the Debye length, which are typically below 1 micron.

The potential of the electric field in the liquid phase is described by the classical Poisson's equation,

$$\nabla^2 \psi^* = -\frac{\rho_E}{\epsilon}, \tag{2}$$

where ρ_E is the bulk charge density. Assuming the Boltzmann distribution for the ion concentrations allows one to rewrite Poisson's equation in the form

$$\nabla^2 \psi^* = -\sum_{k=1}^{N} \frac{n_k^{(0)} e z_k}{\epsilon} \exp\left(\frac{z_k e \psi^*}{k_B T^*}\right). \tag{3}$$

For electric potentials well below the value of $k_B T/e$ (about 25 mV), the right-hand side of Eq. (3) can be linearized, an approach known as the Debye-Hückel approximation. With the Debye length defined by (1), we write the linearized equation in the form

$$\nabla^2 \psi^* = \lambda_D^{-2} \psi^*. \tag{4}$$

With our choice of length scales, this approximation leads to the following leading-order equation for the nondimensional

potential,

$$\psi_{yy} = \kappa^2 \psi. \tag{5}$$

Here the potential is scaled by $q^* \lambda_D/\epsilon$, q^* being the dimensional charge density at the fluid interface, assumed constant and spatially uniform along the interface, with typical value on the order of 0.1mC/m^2, although some experimental studies report much smaller values; see, e.g., Ketelaar and Ajaev [40] for a discussion of experimental results. The substrate charge density $\tilde{q}$, scaled by q^*, is either constant or a prescribed function of the spatial coordinate. These conditions allow us to determine the potential from Eq. (5) and then express its value at the fluid interface, denoted by $\hat{\psi}$, as

$$\hat{\psi} = \frac{\tilde{q} + \cosh(\kappa h)}{\sinh(\kappa h)}, \tag{6}$$

where h is the liquid layer thickness scaled by $\text{Ca}^{1/3} R_0$.

The electrostatic effects in the contact line region are commonly described in terms of the so-called electrostatic component of disjoining pressure, Π_e. Detailed derivations of the general formulas for this quantity can be found, e.g., in the classical book of Derjaguin *et al.* [28] and in Appendix 1 of Kuchin *et al.* [42]. Taking advantage of the small ψ and the fixed charge density condition at the fluid interface, the nondimensional form of Eq. (8) of Ref. [42] reduces to the following simple form,

$$\Pi_e = \frac{Q}{2}(\hat{\psi}^2 - 1). \tag{7}$$

The dimensionless parameter $Q \equiv q^{*2} R_0/(\sigma\epsilon)$, often referred to as the electric Weber number, determines the relative magnitude of the Maxwell stresses at the fluid interface as compared to the surface tension. By substituting Eq. (6) into the formula for Π_e, the latter can be explicitly related to the film thickness via

$$\Pi_e = Q\left[\frac{1 + 2\tilde{q}\cosh(\kappa h) + \tilde{q}^2}{2\sinh^2(\kappa h)}\right]. \tag{8}$$

The structural component of disjoining pressure is neglected in the present study, but the contribution of the London–van der Waals component is retained, leading to the expression for the total disjoining pressure of the form

$$\Pi = \frac{\alpha}{h^3} + \Pi_e, \tag{9}$$

where $\alpha = |A|/(\sigma R_0^2 \text{Ca})$, and A is the Hamaker constant, which measures the contribution of unbalanced London–van der Waals interactions to stresses in thin liquid layers [28,29]. Viscous flow which supplies liquid for evaporation is driven by a combination of the gradients of capillary and disjoining pressure, so the lubrication-type velocity profile [36–38] in the reference frame moving with the contact line at speed U is given by

$$u = -\tfrac{1}{2}(h_{xx} + \Pi)_x (y^2 - 2yh) - U + \tau y. \tag{10}$$

Here we introduced scaled tangential stress τ at the interface which is due to a combination of the Marangoni effect, i.e., the dependence of surface tension on temperature, and the action of electric field on the interfacial charges. The latter term is often neglected, but for small Ca it is actually of the same asymptotic order as the electrostatic contribution to the normal stress [34,40,43]. Accounting for both sources of variation of the interfacial shear stress leads to the following expression:

$$\tau = -\kappa^{-1} Q(\hat{\psi}_h h_x + \hat{\psi}_x) - \text{Ma}\, T^i_x, \tag{11}$$

where $\text{Ma} = \gamma \Delta T/(\sigma \text{Ca}^{1/3})$ is the modified Marangoni number expressed in terms of the slope γ of $\sigma(T)$ curve, T^i is the scaled interfacial temperature, defined in terms of its dimensional counterpart and the equilibrium saturation temperature T_s^* as

$$T^i = \frac{T^{i*} - T_s^*}{\Delta T}. \tag{12}$$

In the derivation of Eq. (11) we followed the same steps as described in detail in two recent studies [33,40]. Both capillary and electrostatic effects result in the shift of the equilibrium saturation temperature. In the constant-curvature meniscus region away from the apparent contact line, these effects are small so that the equilibrium saturation temperature there is actually close to the value that corresponds to a flat liquid-vapor interface with negligible effect of electrical charges. However, in the apparent contact line region, the high curvature and relatively large disjoining pressure lead to significant departures from the local equilibrium saturation temperature. In nondimensional terms, the shift is characterized by the nondimensional parameter $\delta = \sigma T_s^*/(\rho R_0 \Delta T \mathcal{L})$. Furthermore, departures from thermodynamic equilibrium due to phase change are measured by the parameter $K = kT_s^* \sqrt{2\pi \bar{R} T_s^*}/(2\rho_v R_0 \mathcal{L}^2 \text{Ca}^{1/3})$ that emerges from the nondimensional form of the classical Hertz-Knudsen relation [44]. Detailed asymptotic derivation of this relation from the kinetic gas theory can be found, e.g., in Chap. 6 of Ref. [38]. The pressure and temperature jumps obtained by direct kinetic simulation are discussed in Polikarpov *et al.* [45]. Experimental investigations of this interfacial phenomenon are presented in [46]. In the present study we use the classical approach, which is valid when the mass flux in the energy balance is maximal and the heat flux in vapor phase is negligible [45,46]. Combining the boundary condition for the pressure drop at the liquid-vapor interface with the Hertz-Knudsen equation leads to the following relation between the evaporative mass flux and temperature at the liquid-vapor interface:

$$KJ = T^i - \delta(h_{xx} + \Pi). \tag{13}$$

Suppose the dimensional solid wall temperature is T_w^*, which is either constant or a specified function of the coordinate. Let us define the corresponding nondimensional quantity according to

$$T_w = \frac{T_w^* - T_s^*}{\Delta T}. \tag{14}$$

In the framework of our lubrication-type model, the temperature profile across the liquid layer is linear and therefore the interfacial and the solid wall temperatures are related by

$$T^i = T_w - Jh. \tag{15}$$

Substituting this expression into Eq. (13) leads to

$$J = \frac{T_w - \delta(h_{xx} + \Pi)}{K + h}. \tag{16}$$

The specified value of T_w implies that the model does not account for heat conduction in the solid substrate, an effect which may result in reduction of the heat flux and can in principle be incorporated into our model using the approach discussed, e.g., in Schweikert *et al.* [47]. For a heated wall at temperature T_w evaporation is suppressed when the value of J in Eq. (16) is zero, meaning that $\delta\Pi(h_0) = T_w$. If this equation has a positive solution h_0, then the ultrathin flat film of thickness h_0 is expected to form on the substrate. For disjoining pressure dominated by the London–van der Waals component, h_0 can always be found as long as the Hamaker constant A is negative.

The integral mass balance in nondimensional form in the lubrication-type framework is given by

$$h_t + J + \left(\int_0^h u\,dy\right)_x = 0. \tag{17}$$

Substituting the velocity profile from Eq. (10) together with Eq. (11) into the integral mass balance leads to the evolution equation,

$$h_t - U h_x + J + \frac{1}{3}\Big[h^3\Big(h_{xx} + \frac{\alpha}{h^3} + \Pi_e\Big)_x\Big]_x - \frac{1}{2}\Big[h^2\big(\kappa^{-1}Q(\hat{\psi}_h h_x + \hat{\psi}_x) + \mathrm{Ma}\,T_x^i\big)\Big]_x = 0. \tag{18}$$

The boundary conditions for this equation are

$$h(0,t) = h_m, \quad h_{xx}(0,t) = 1, \quad h_x(L,t) = h_{xxx}(L,t) = 0, \tag{19}$$

where h_m is chosen large enough so that the effects of disjoining pressure near the left endpoint of the domain are negligible; in a typical simulation below, $h_m = 20$ and $L = 10$. The specified value of h_{xx} reflects the condition of constant curvature of the meniscus away from the wall, while the two conditions at $x = L$ are formulated to ensure that the interface remains flat in the ultrathin-film region. Equation (18) with these boundary conditions has been solved numerically using the finite-difference method with DVODE software package [48]. Local mesh refinement is implemented near the contact line.

III. MOTION OVER HOMOGENEOUS SUBSTRATE

In order to better understand the role of different factors in the determination of the interface shape and flow structure near an apparent contact line, let us first consider its motion over the substrate with spatially homogeneous properties. In the reference frame moving with the speed U, numerical simulations indicate that, following a short transient, a steady state is reached. The resulting shape of the interface in the apparent contact line region is shown by the solid line in Fig. 2(a). The interface has nearly constant curvature near the left end of the domain but then flattens near $x \sim 4.1$, indicating a transition to the flat ultrathin film. The dashed line in the plot indicates the constant-curvature line which matches the behavior of the interface near the left endpoint of the computational domain. The point of intersection of this line with the horizontal axis is used to define the position of the apparent contact line, x_{CL}, as is common in the literature;

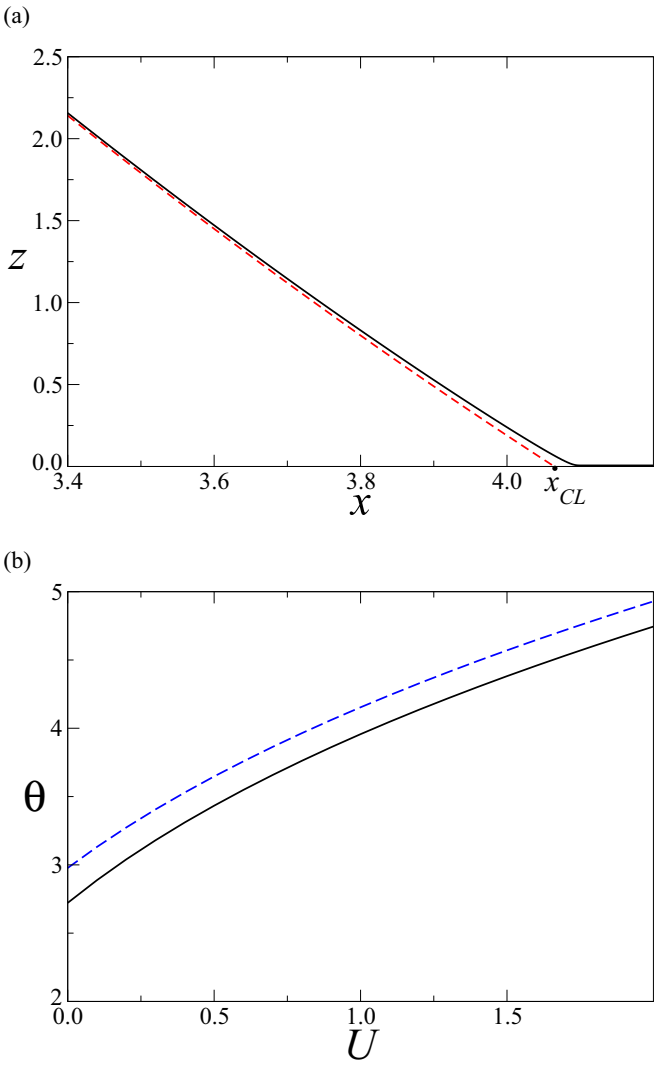

FIG. 2. Numerical results for homogeneous substrates: (a) steady interface shape in the apparent contact line region in the reference frame moving with the speed $U = 0.1$ for $\tilde{q} = 0$, with dashed line showing the constant-curvature fit to the interface; (b) apparent contact angle as a function of nondimensional speed for $\tilde{q} = 0$ (solid line) and $\tilde{q} = -1$ (dashed line). For all simulations, $\mathrm{Ma} = Q = 1$, $\kappa = 5$, $K = 0.01$, $\alpha = 10^{-5}$, $T_w = 0.1$, $\delta = 2 \times 10^{-4}$.

the magnitude of the dashed line slope at the point of intersection defines the apparent contact angle, θ. Alternatively, the contact line position can be defined by the maximum of local curvature; we verified that both definitions lead to similar conclusions about the contact line dynamics.

The rapid change of the interfacial curvature near $x \sim 4.1$ in Fig. 2(a) implies that the scaled capillary pressure, $-h_{xx}$, is significant in that region. However, the disjoining pressure, negligible near the left end of the computational domain, can become large in the contact line region. Indeed, in order to suppress evaporation in the flat thin film, i.e., ensure that the evaporative flux J is zero, the disjoining pressure there has to satisfy $\Pi = T_w/\delta$. Thus, both capillary and disjoining pressure gradients contribute to the flow that supplies liquid into the transition region, as needed to maintain evaporation

and continuous advancement of the contact line. There are also two additional physical effects due to shear stresses, as seen in Eq. (11); let us discuss their relative significance. The Marangoni stresses are expected to make a small contribution for uniformly heated substrates, since the interfacial temperature gradient is proportional to the small parameter δ; we verified this by running the code at different values of Ma and observing the change in the interface shape to be very small. To investigate the contribution of electrostatic effects to the shear stress, we use an estimate $\hat{\psi} \sim (\kappa h)^{-1}$ in place of Eq. (6), as appropriate for small film thickness in the transition region and for $\tilde{q}$ near zero. The component of the flow rate due to electrostatically induced shear stress in Eq. (18) can then be estimated by

$$\frac{Qh^2}{2\kappa}\hat{\psi}_h h_x \approx -\frac{Q}{2\kappa^2}h_x. \tag{20}$$

This flow contribution is comparable to that from the electrostatic disjoining pressure gradient, although it can still be negligible if the London–van der Waals component of disjoining pressure dominates, i.e., if $\Pi_x \sim -3\alpha h_x/h^4$ is large compared to other pressure gradients in the system. This can happen when the electric Weber number Q is small or when the inverse scaled Debye length κ is large.

Let us now discuss how the apparent contact angle θ, defined by the slope of the dashed line in Fig. 2(a) at $x = x_{CL}$, depends on dynamics and the substrate properties. We plot the angle as a function of the contact line speed in Fig. 2(b) for different values of the substrate charge density. The contact angles become larger when $\tilde{q}$ is increased and as the contact line speed increases. It is also clear from the plot that the contact angle is not very sensitive to $\tilde{q}$, as the difference between the two curves in Fig. 2(b) is rather small. The contact-angle correction is approximately the same for all values of the velocity investigated, which is not surprising given that $\tilde{q}$ characterizes a static property of the substrate not likely to be strongly coupled to flow dynamics.

When a contact line advances under the isothermal conditions, the cube of the dynamic contact angle is a linear function of $\mu U^*/\sigma$ for sufficiently small capillary numbers [17]. Our result in Fig. 2(b) shows qualitatively similar dependence since the angle increases with the speed and the curve $\theta(U)$ is concave down. However, we did not observe quantitative agreement with the isothermal results. This is not surprising, since our apparent contact angle value depends on complicated coupling between flows generated by contact line advancement and by the evaporation.

IV. INTERACTION WITH WETTABILITY DEFECT

Let us now consider a situation when an advancing contact line approaches an isolated wettability defect, which is incorporated into our model through the spatially dependent disjoining pressure, based on Eq. (8) with

$$\tilde{q} = q_d \exp\left[-\frac{(x - x_d)^2}{l_d^2}\right]. \tag{21}$$

Thus, the defect is basically a region of substrate where surface charges are presently characterized by three parameters: the maximum charge density q_d, location x_d, and the characteristic width l_d. Highly localized defects correspond to small values of the parameter l_d. While we focus on a specific method for wetting properties modification, i.e., surface charges, the conclusions are expected to be applicable to other situations when the disjoining pressure is spatially dependent.

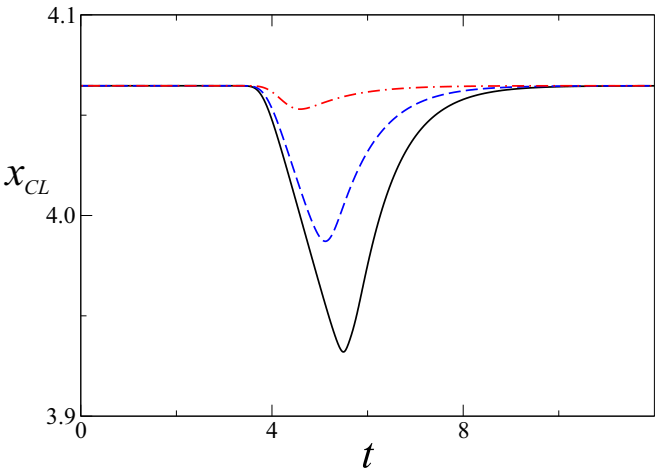

FIG. 3. Position of the advancing contact line as a function of time for $U = 0.1$, $l_d = 0.03$, and different defect amplitudes, $q_d = -1$ (solid line), $q_d = -0.5$ (dashed line), and $q_d = -0.1$ (dot-dashed line). All other parameter values are the same as in Fig. 2.

The substrate temperature for now is assumed uniform, an assumption to be revisited later in the present study. One may argue that this assumption is not realistic since the local change of chemical properties of the substrate should also be accompanied by the change in the thermal properties. However, there are well-known experimental techniques which allow one to modify the wetting properties only, e.g., by using very thin layers of coating [15,49].

A. Contact line dynamics

We solve Eq. (18) numerically with the initial conditions corresponding to the defect being far ahead of the contact line, $x_d = 4.5$. The position of the apparent contact line x_{CL} is then found from the numerical interface shape as illustrated in Fig. 2(a), i.e., as the point of intersection of the constant-curvature fitting meniscus with the substrate and plotted as a function of time in Fig. 3. The position is recorded in moving reference frame, so the negative slope corresponds so the slowdown of the advancing contact line. This slowdown is followed by an acceleration of the contact line after the defect is passed, both features being consistent with the experimentally observed stick-slip behavior. Comparison between the three lines in Fig. 3 illustrates the importance of the defect amplitude: the maximum of the slope magnitude and thus the degree of contact line slowdown decrease with the decrease in the magnitude of q_d. Figure 3 also shows that the total time of interaction of the contact line with the defect, estimated as the time it takes to recover the original contact line speed from the moment when the slowdown started, increases with defect amplitude.

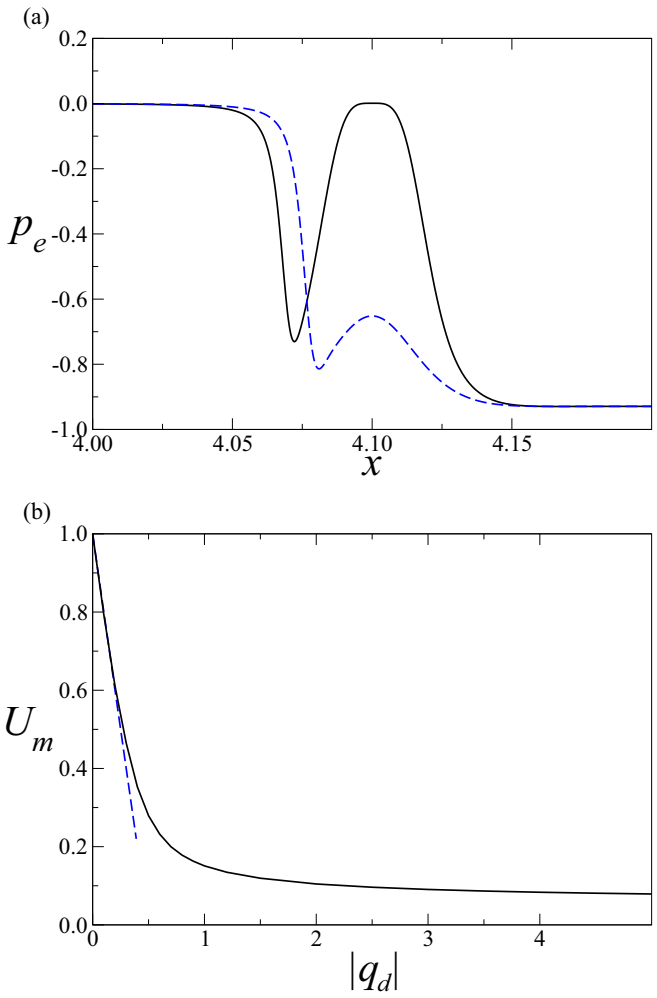

FIG. 4. (a) The electrostatic contribution to the effective pressure in the film $p_e = -\delta\Pi_e/T_w$ as a function of the coordinate for $q_d = -1$ (solid line), $q_d = -0.5$ (dashed line); (b) minimum contact line speed recorded during the interaction of the contact line with the defect is shown as a function of defect amplitude (for negative q_d); dashed line shows the prediction of the approximate model, Eq. (23).

Let us now discuss the physical explanation of the numerical results illustrated in Fig. 3. When the defect is far ahead of the contact line, the situation is similar to the homogeneous substrate case, Sec. III; liquid supply into the transition region is maintained by capillary and disjoining pressure gradients together with the tangential stresses. When the contact line region encounters the defect, the newly introduced charges in the electrical double layer near the solid partially neutralize the charges in the film and the osmotic pressure is decreased, meaning that the local effective pressure (including hydrodynamic and osmotic components) is increased. This pressure acts against the flow of the liquid into the apparent contact line region, as illustrated in Fig. 4(a). Both lines in the figure represent the electrostatic contribution to the effective pressure in the film, scaled by the maximum disjoining pressure, as a function of the coordinate but for different defect amplitudes. The pressure barrier introduced by the defect naturally increases as the amplitude is increased, as seen by comparing the solid and dashed lines in the figure. The contact line slowdown becomes more significant since the liquid flow has to overcome higher stresses, consistent with the result shown in Fig. 3.

To further elucidate the role of the defect amplitude, we plot the minimum contact line speed U_m during the interaction with the defect, scaled by U, as a function of the magnitude of q_d in Fig. 4(b), solid line. For higher defect amplitudes, the contact line slows down dramatically almost to the point of pinning, while weak defects can be passed with only slight decrease in the velocity, so that $U_m \sim 1$. For the latter case, a simple estimate of the degree of the slowdown can be obtained using the following arguments. The local change in the disjoining pressure induced by the presence of the defect is estimated from Eq. (8) as

$$\Delta\Pi_e \sim Qq_d(\kappa h)^{-2} \tag{22}$$

for $\kappa h \ll 1$ and $|q_d| \ll 1$. Assuming the defect width is comparable to the length scale of the interface shape change in the transition region, which is typically the case in our simulations, we can then state that the pressure gradient driving the flow into the contact line region reduces by a factor of $1 - 2|q_d|$ due to the defect. If the corresponding change in the flow rate is compensated by the change in the speed of the contact line, then the contact line speed has to decrease by the same factor, leading to the following simple nondimensional estimate:

$$U_m = 1 - 2|q_d|. \tag{23}$$

The dashed line in Fig. 4(b) represents this equation and agrees with the numerical results surprisingly well, even for $|q_d|$ as large as ~0.3. Note that the argument does not account for complicated nonlinear coupling between contact line motion, evaporation, viscous flow, and tangential stresses, and thus is expected to break down for sufficiently large $|q_d|$, which is indeed seen in Fig. 4(b). Clearly, at large defect amplitudes the contact line slows down, basically to the point of pinning, in qualitative agreement with experimental data showing that only sufficiently strong defects lead to contact line pinning. In our model, complete pinning ($U_m = 0$) is not seen since the Hamaker constant is not affected by the defect and thus the London–van der Waals component of disjoining pressure continues to support slow contact line advancement even near the defect. We verified that U_m can be further reduced below the values seen in Fig. 4(b) by making α smaller.

Based on the estimate of U_m, Eq. (23), the total time of interaction of the contact line with defect is given by $l_d/[U(1 - 2|q_d|)]$. Note that this value, consistent with the result in Fig. 3, can be an order of magnitude larger than expected from the rough estimate, l_d/U, not accounting for the contact line slowdown.

Estimates such as Eq. (23) highlight the crucial role of the defect amplitude for the dynamics and suggest that the significance of the defect width l_d is less important, a conclusion supported by our numerical simulations. For example, the results in Fig. 5 show that the change of the defect width by a factor of 3 results in only a relatively small change in the contact line dynamics. Comparing the two curves in the figure, it is clear that more localized defects result in more contact line slowdown (indicated by the higher slope of the

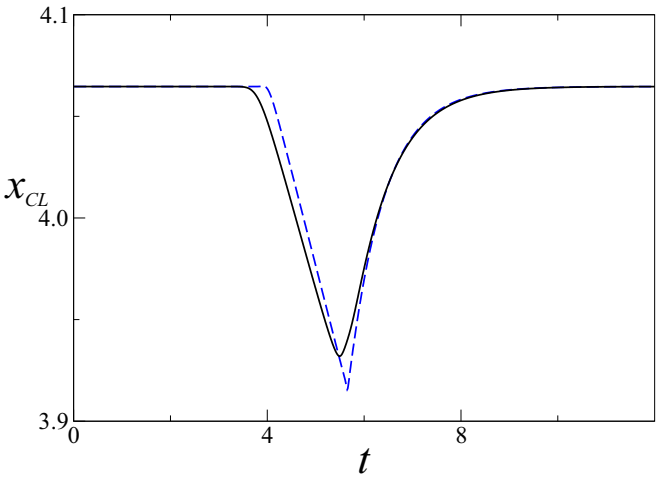

FIG. 5. Position of the advancing contact line as a function of time for $T_w = 0.1$, $q_d = -1$, and different defect widths, $l_d = 0.03$ (solid line) and $l_d = 0.01$ (dashed line).

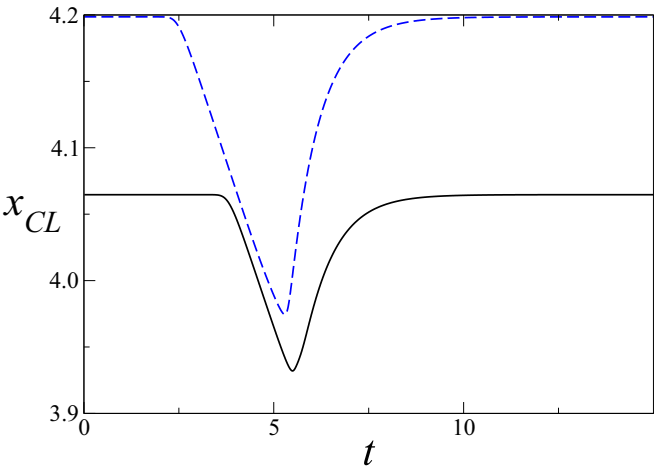

FIG. 6. Position of the advancing contact line as a function of time predicted by the solution of Eq. (18), solid line, and by the simplified version of the same model obtained by setting the shear stress τ to zero, dashed line.

dashed line) for the same defect amplitude at the first stage of interaction with the defect, while the contact line relaxation to the original speed at the second stage of the process is almost unaffected. The latter conclusion is not surprising, since the timescale of relaxation is determined by the timescale of viscous flow in the film after the contact line already passed the defect.

B. Shear stress at the interface

The shear stresses at the liquid-vapor interface, represented by Eq. (11) above, are often neglected in simulations of moving contact lines. However, our estimates of their relative importance in Sec. III suggests that even for the homogeneous substrates the condition of negligible shear stress is often not satisfied; we expect the shear-stress contribution to become even more significant when an additional short length scale is introduced due to the defect. It is therefore instructive to investigate the role of shear stresses in contact line dynamics in the presence of evaporation. Figure 6 illustrates the predictions of the contact line motion by our model and a simplified version of the same model with the interfacial stress τ set to zero. We observe that the simplified model overestimates the degree of the pull-back by the defect and that the discrepancy can be significant. Both the minimum contact line speed and the total time of interaction with the defect are not predicted correctly.

To better understand the role of the shear stress in the overall dynamics of the system, let us start by discussing the case of a homogeneous substrate. The electric potential $\hat{\psi}$ from Eq. (6) increases as the interface approaches the substrate, i.e., in the positive x direction. Based on Eq. (11), the interfacial stress vector is in the opposite direction. This can be explained in physical terms by electrical charges near the interface interacting with their electrostatic images which have the same sign (due to zero derivative condition on the potential at the wall); thus there is repulsive interaction pushing the interfacial charges away from the substrate. An additional smaller contribution due to the Marangoni effect acts in the same direction since the interfacial temperature is increased as the hot wall is approached, see Eq. (10). The flow generated by all these tangential stresses is in the direction opposite to the main flow supplying the liquid into the region of high evaporation. By artificially removing the tangential stress component, we eliminate these extra contributions and the contact line is expected to shift to the right, as indeed is seen in Fig. 6.

When a defect is introduced, with no contribution from shear-induced flow, all adjustments for altered local wetting properties are made in the pressure gradient value, meaning that larger changes in pressure and thus stronger interface deformation can be expected. This results in a larger shift in the apparent contact line position, as seen in Fig. 6.

C. Effects of evaporation

One of the key features of the proposed model is substrate heating and the resulting evaporative mass loss which is coupled to liquid flow. To the best of our knowledge, the interaction of advancing contact lines with defects in the presence of evaporation has not been addressed in the literature previously, despite its importance for numerous heat transfer applications such as boiling and spray cooling. In order to get some insight into how the stick-slip motion can be affected by the evaporation, we carried out numerical simulations at different values of the substrate superheat.

When the defect is far ahead of the contact line, the steady-state solutions will be different depending on the superheat. In addition to changes in the local structure of the solutions, there is also a shift in the contact line location which is purely due to the boundary condition of the specified thickness at the left end of the computational domain, a shift which has no physical significance. Therefore, we present all of our results in terms of the contact line position $\hat{x}_{CL}$ measured relative to its value for the homogeneous substrate. The simulation results for a range of values of T_w between 0.05 and 0.3 show that the increase in the superheat has little effect on the slope of the line, i.e., the value of U_m, at the first stage of the process

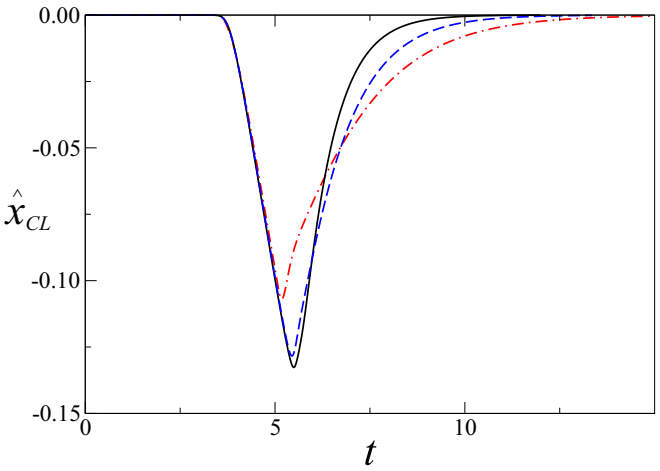

FIG. 7. Shift in the position of the advancing contact line as a function of time for $T_w = 0.02$ (dot-dashed line), $T_w = 0.05$ (dashed line), and $T_w = 0.1$ (solid line).

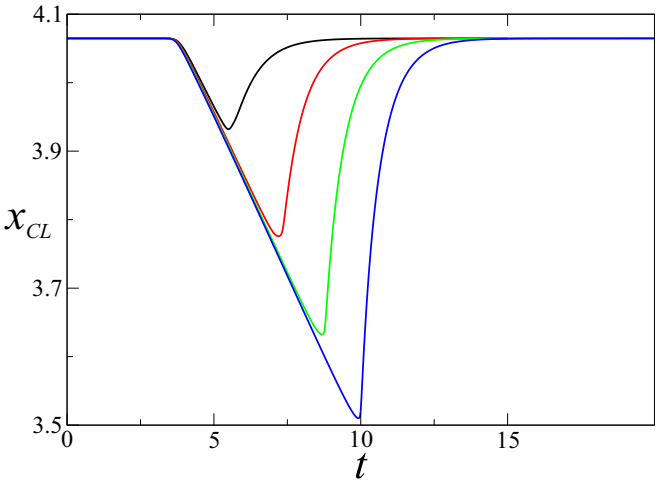

FIG. 8. Position of the advancing contact line as a function of time for the values of T_d equal to (from top curve to bottom) 0.1, 0.15, 0.2, 0.25 with $T_{w0} = 0.1$, $q_d = -1$, $l_d = 0.03$.

of contact line–defect interaction, as seen by comparing the solid and dashed lines in Fig. 7. This is not surprising based on the arguments made in Sec. IV A about the defect amplitude being the key quantity determining the degree of the contact line slowdown. The relaxation of the interface after the defect passed proceeds faster for higher temperature, as the interface can now adjust to the equilibrium shape not only via surface tension effects but also via evaporative mass transport. The evaporative mechanism can be expected to weaken significantly at lower temperatures, which was indeed observed in our simulations for T_w near 0.02 and below, illustrated by the dot-dashed line in Fig. 7. At these low temperatures, the degree of the contact line pullback during the interaction with the defect also starts to decrease slightly.

V. NONUNIFORM SUBSTRATE TEMPERATURE

Nonuniformity of the substrate chemical properties often leads to the nonuniformity of the thermal properties as well, unless special care is taken to avoid the latter. Furthermore, substrate temperature can be highly nonuniform in electronics cooling applications, often characterized by the formation of the so-called hot spots [50]. When such a substrate is cooled by a thin-film flow [51,52], the film can rupture, leading to formation of moving contact line on a substrate with highly nonuniform temperature. The objective of the present section is to analyze how the *local* change in the substrate temperature could lead to changes in the contact line motion and conditions of pinning. We take the Gaussian-type temperature profile

$$T_w = T_{w0} + (T_d - T_{w0}) \exp\left[-\frac{(x - x_d)^2}{l_d^2}\right], \qquad (24)$$

with the maximum temperature T_d in the middle of the defect assumed to be higher than the value away from it, T_{w0}. Local increase in the substrate temperature is shown to increase the degree of contact line pinning significantly, as illustrated in Fig. 8. The overall time of the interaction of the contact line with the defect also increased substantially. We attribute these changes to the Marangoni effect pushing liquid away from the hotter region encountered during the contact line advancement. The Marangoni effect was rather small previously due to the interface temperature gradient being proportional to the small parameter δ. However, for nonuniform substrate temperature the term T_w in Eq. (15) is also a function of the spatial coordinate and thus contributes to the temperature gradient; that term is independent from δ and is not expected to be small.

VI. CONCLUSIONS

We investigated the interaction of advancing contact lines with defects. For most of our study, we focus on the situation when the wetting properties of the substrate are changed locally, e.g., by the presence of electrical surface charges, but the temperature and thermal properties remain uniform. The defect amplitude, a measure of the magnitude of the change in the local wetting properties, is identified as the key parameter in the dynamics of the contact line. For the case of local modification of the substrate properties by surface charges, the amplitude can be interpreted simply as the local scaled charge density. Stick-slip type behavior is found for sufficiently large defect amplitudes; weak defects result only in slight reduction of the contact line speed. For the latter case, a simple analytical model predicts linear decrease of contact line velocity with the defect amplitude; the analytical formula matches the numerical result in the region where both are applicable. The contact line dynamics is much less sensitive to the changes in the defect width and the substrate temperature, as long as the latter remains spatially uniform.

The classical disjoining pressure models involve modifications in the normal stress balance at the interface but not in the shear stress. Our results point to the limitations of this approach, especially for the interaction between a contact line and a highly localized defect. The tangential stress is shown to be comparable to the normal stress contributions of the electrostatic forces. Its relative importance increases as the

Debye length is increased. Models neglecting the shear-stress effects at the interface tend to overestimate the degree of the vapor-liquid interface deformation.

The effect of local change in the substrate temperature is investigated and shown to result in a dramatic increase of the degree of the contact line pull-back by the defect and the overall time of the interaction. This dynamics is explained by the role of the Marangoni stresses, which induce the flow away from a hot region encountered during the advancement of the contact line, a different mechanism of contact line pinning not related to the wetting properties of the substrate.

Our results indicate that contact line motion is very sensitive even to small defects on the substrate. Thus, accurate experimental recording of contact line velocity can provide valuable information about the chemical properties and degree of uniformity of the substrate on micro- or even nanoscale. Such properties, including the presence of defects, can be investigated by a variety of methods such as scanning electron microscopy, but these methods require much more sophisticated equipment than simple experimental study of contact line motion.

ACKNOWLEDGMENT

This study was supported by the Russian Science Foundation (Project No. 19-19-00695).

[1] C. Sodtke and P. Stephan, Int. J. Heat Mass Transfer **50**, 4089 (2007).
[2] J. Kim, Int. J. Heat Fluid Flow **28**, 753 (2007).
[3] P. C. Stephan and C. Brandt, Heat Transfer Eng. **25**, 78 (2004).
[4] V. K. Dhir, G. R. Warrier, and E. Aktinol, J. Heat Transfer **135**, 061502 (2013).
[5] A. Urbano, S. Tanguy, G. Huber, and C. Colin, Int. J. Heat Mass Transf. **123**, 1128 (2018).
[6] V. Srinivasan, V. Marty-Jourjon, S. Khandekar, F. Lefèvre, and J. Bonjour, Int. J. Heat Mass Transf. **89**, 176 (2015).
[7] S. Lips, V. Sartre, F. Lefevre, S. Khandekar, and J. Bonjour, Interfacial Phenom. Heat Transf. **4**, 33 (2016).
[8] E. F. Médici and J. S. Allen, Int. J. Heat Mass Transf. **65**, 779 (2013).
[9] S. S. Panchamgam, J. L. Plawsky, and P. C. Wayner Jr., Exp. Therm. Fluid Sci. **30**, 745 (2006).
[10] S. S. Panchamgam, A. Chatterjee, J. L. Plawsky, and P. C. Wayner Jr., Int. J. Heat Mass Transfer **51**, 5368 (2008).
[11] M. Potash and P. C. Wayner Jr., Int. J. Heat Mass Transfer **15**, 1851 (1972).
[12] S. Moosman and G. M. Homsy, J. Colloid Interface Sci. **73**, 212 (1980).
[13] P. A. Raghupathi and S. G. Kandlikar, Int. J. Heat Mass Transf. **95**, 296 (2016).
[14] V. S. Ajaev and O. A. Kabov, Int. J. Heat Mass Transfer **108**, 918 (2017).
[15] A. R. Betz, J. Xu, H. Qiu, and D. Attinger, Appl. Phys. Lett. **97**, 141909 (2010).
[16] H. Tavana, G. Yang, C. M. Yip, D. Appelhans, S. Zschoche, K. Grundke, M. L. Hair, and A. W. Neumann, Langmuir **22**, 628 (2006), .
[17] P. G. de Gennes, Rev. Mod. Phys. **57**, 827 (1985).
[18] E. B. Dussan, Annu. Rev. Fluid Mech. **11**, 371 (1979).
[19] H. Hervet and P. G. de Gennes, C.R. Acad. Sci. Paris II **299**, 499 (1984).
[20] H. P. Kavehpour, B. Ovryn, and G. H. McKinley, Phys. Rev. Lett. **91**, 196104 (2003).
[21] C. Huh and L. Scriven, J. Colloid Interface Sci. **35**, 85 (1971).
[22] H. P. Greenspan, J. Fluid Mech. **84**, 125 (1978).
[23] P. D. Spelt, J. Comput. Phys. **207**, 389 (2005).
[24] S. Afkhami, S. Zaleski, and M. Bussmann, J. Comput. Phys. **228**, 5370 (2009).
[25] L. W. Schwartz, Langmuir **14**, 3440 (1998).
[26] U. Thiele and E. Knobloch, Phys. Rev. Lett. **97**, 204501 (2006).
[27] P. Beltrame, P. Hänggi, and U. Thiele, Europhys. Lett. **86**, 24006 (2009).
[28] B. V. Derjaguin, N. V. Churaev, and V. M. Muller, *Surface Forces* (Plenum Press, NY, 1987).
[29] J. N. Israelachvili, *Intermolecular and Surface Forces*, 3rd ed. (Academic Press, San Diego, 2011).
[30] F. Brochard-Wyart, J. M. Di Meglio, D. Quere, and P. G. De Gennes, Langmuir **7**, 335 (1991).
[31] V. S. Ajaev, T. Gambaryan-Roisman, and P. Stephan, J. Colloid Interface Sci. **342**, 550 (2010).
[32] A. Sharma and A. T. Jameel, J. Colloid Interface Sci. **161**, 190 (1993).
[33] E. Gatapova, O. A. Kabov, and V. S. Ajaev, Int. J. Heat Mass Transfer **142**, 118355 (2019).
[34] C. Ketelaar and V. S. Ajaev, Phys. Rev. E **91**, 052403 (2015).
[35] S. G. Kandlikar, Exp. Therm. Fluid Sci. **26**, 389 (2002).
[36] A. Oron, S. H. Davis, and S. G. Bankoff, Rev. Mod. Phys. **69**, 931 (1997).
[37] R. V. Craster and O. K. Matar, Rev. Mod. Phys. **81**, 1131 (2009).
[38] V. S. Ajaev, *Interfacial Fluid Mechanics: A Mathematical Modeling Approach* (Springer, New York, 2012).
[39] Y. Kabova, V. Kuznetsov, O. Kabov, T. Gambaryan-Roisman, and P. Stephan, Int. J. Heat Mass Transfer **68**, 527 (2014).
[40] C. Ketelaar and V. S. Ajaev, Phys. Fluids **27**, 112110 (2015).
[41] V. S. Ajaev and G. M. Homsy, J. Colloid Interface Sci. **240**, 259 (2001).
[42] I. V. Kuchin, O. K. Matar, R. V. Craster, and V. M. Starov, Soft Matter **10**, 6024 (2014).
[43] S. R. Maduar, A. V. Belyaev, V. Lobaskin, and O. I. Vinogradova, Phys. Rev. Lett. **114**, 118301 (2015).
[44] R. W. Schrage, *A Theoretical Study of Interface Mass Transfer* (Columbia University Press, New York, 1953).
[45] A. Polikarpov, I. Graur, E. Gatapova, and O. Kabov, Int. J. Heat Mass Transfer **136**, 449 (2019).
[46] E. Y. Gatapova, I. A. Graur, O. A. Kabov, V. M. Aniskin, M. A. Filipenko, F. Sharipov, and L. Tadrist, Int. J. Heat Mass Transfer **104**, 800 (2017).

[47] K. Schweikert, A. Sielaff, and P. Stephan, Interfacial Phenom. Heat Transf. **7**, 269 (2019).

[48] A. C. Hindmarsh, P. N. Brown, K. E. Grant, S. L. Lee, R. Serban, D. E. Shumaker, and C. S. Woodward, ACM Trans. Mathematical Software (TOMS) **31**, 363 (2005).

[49] B. Sobac and D. Brutin, Langmuir **27**, 14999 (2011).

[50] A. Bar-Cohen, J. R. Sheehan, and E. Rahim, Microgravity Sci. Technol. **24**, 1 (2012).

[51] E. Y. Gatapova and O. A. Kabov, Int. J. Heat Mass Transfer **51**, 4797 (2008).

[52] O. A. Kabov, D. V. Zaitsev, V. V. Cheverda, and A. Bar-Cohen, Exp. Therm. Fluid Sci. **35**, 825 (2011).